

Mesoscopic modelling of concrete under impact

R.R. Pedersen, A. Simone, M. Stroeven & L.J. Sluys

Delft University of Technology, Faculty of Civil Engineering and Geosciences, Delft, The Netherlands

ABSTRACT: We present a mesoscopic model for the analysis of tensile failure of concrete under impact loading. Rate dependency is incorporated through viscosity terms in the constitutive formulation. The model is applied to mesoscopic analyses of three-phase mesoscopic descriptions of concrete consisting of elastic aggregates, inelastic bulk material and interfacial transition zones (ITZs). The tensile strength of the ITZ influences the global strength and the shape of the final failure zone. Different aggregate distributions affect the diffuse failure pattern but the change of the overall strength is less significant. The numerical responses are compared with experimental results from a gravity driven Split Hopkinson bar test setup.

1 INTRODUCTION

Experimental observations have provided an insight into the complicated fracture process of concrete in statics and dynamics (Reinhardt and Weerheijm 1991; Rossi et al. 1992). Concrete is a heterogeneous brittle material that fractures via the formation, growth and coalescence of microcracks. Furthermore, the failure process is dependent on the loading rate. Micro inertia of the material adjacent to propagating micro cracks and moisture in the capillary pores characterise the rate dependent behaviour of concrete. A representative computational model of concrete in dynamics must include these features.

A more realistic description of fracture processes ranging from diffuse failure to localisation and final discrete failure can be described by means of an explicit model of the mesostructure. In dynamics the modified inertia effect and the geometrical dispersive characteristic are other consequences of the mesoscopic model. For the constituents in the mesostructure we apply a rate dependent constitutive model.

Realistic homogeneous macroscopic models for heterogeneous materials incorporate information from the lower scales. A successful constitutive theory is the microplane theory (Bažant and Prat 1988; Carol and Bažant 1997). This approach is extended including damage and plasticity formulations by D'Addetta et al. (2002) and Kuhl et al. (2000). Also enhanced continuum theories implicitly incorporate lower scale effects by introducing a length scale parameter. An example of these theories is the Cosserat continuum (Mühlhaus 1989) in which rotational degrees of freedom are included to account

for the non-local effects due to the motion of the microstructures. Discrete models exist which are based on Voronoi cell representations of the heterogeneous structure. In these models, a beam lattice network is used to model the cohesive and compressive forces between the neighbouring cells (Bolander and Sukumar 2005; Nagai et al. 2004; Ibrahimbegovic and Delaplace 2003; Schlangen and van Mier 1992). The cohesive crack methodology (Camacho and Ortiz 1996) is also applied at a mesoscopic level (Maiti et al. 2005; Tijssens et al. 2001; Carol et al. 2001).

The mesoscopic problem is solved here using an embedded multiple scale approach. Therefore, the different constituents are modelled explicitly and we apply an idealised geometrical model for the mesoscale consisting of matrix and aggregates surrounded by an interfacial transition zone. The constitutive model used for the constituents is based on thermodynamics of chemically reactive porous media (Lackner et al. 2002; Sercombe et al. 2000; Ulm and Coussy 1995). A viscoelastic model, coupled to a viscoplastic damage model (Simone and Sluys 2004), accounts for the strengthening effect associated with the viscous phenomenon due to moisture. The viscoplastic part contributes to an additional rate effect in the failure zone which is linked to inertia effects.

In this contribution, we focus on the influence of aggregate distribution and strength of the interfacial transition zone. A gravity driven Split Hopkinson Bar test setup is employed to determine the moisture dependent tensile strength (Vegt et al. 2006). A comparison is made between experimental results and numerical estimations for different values of the parameter

governing the viscosity in the bulk material.

2 MATERIAL MODEL

The bulk material and the material in the ITZ obey a viscoelastic viscoplastic damage model which is briefly described next. We assume a strain decomposition of the type

$$\boldsymbol{\epsilon} = \boldsymbol{\epsilon}^e + \boldsymbol{\epsilon}^{\text{ve}} + \boldsymbol{\epsilon}^{\text{vp}} \quad (1)$$

where the strain tensor is split into the elastic, the viscoelastic and the viscoplastic parts. Here we follow Ju (1989) in coupling plasticity and damage and by making use of the effective stress concept and the hypothesis of strain equivalence. This approach does not pose any restriction on the nature of the plastic moduli, apart from the requirement of formulating the plastic moduli in the effective stress space. Therefore, rate-dependent plasticity models, which preserve well-posedness of the governing equations in the softening regime, can be coupled to damage. A quantity in the effective stress space will be denoted by a superimposed tilde.

In the context of a numerical procedure, the stress update relation at the end of a time step for the combined model reads

$$\boldsymbol{\sigma}_{n+1} = (1 - \omega_{n+1}) \tilde{\boldsymbol{\sigma}}_{n+1} \quad (2)$$

where $\boldsymbol{\sigma}$ is the Cauchy stress tensor and ω ($0 \leq \omega \leq 1$) a damage variable which is updated through

$$\omega_{n+1} = \alpha \left(1 - e^{-\beta \kappa_{n+1}} \right). \quad (3)$$

α and β are parameters regulating the asymptotic value of damage and the slope of the damage evolution law, respectively, while κ_{n+1} is a measure of the deformation cumulated in the plastic regime.

The viscoelastic strain contribution is expressed in a rate form as

$$\dot{\boldsymbol{\epsilon}}^{\text{ve}} = \chi \mathbf{b}, \quad (4)$$

where χ is the equivalent viscoelastic strain and \mathbf{b} is defined as

$$\mathbf{b} = \tilde{\mathbf{s}} / |\tilde{\mathbf{s}}|, \quad (5)$$

with $\tilde{\mathbf{s}}$ the deviatoric stress tensor. The equivalent viscoelastic strain obeys the relation Sercombe et al. (2000, eq. (56))

$$\eta_1 \frac{\partial \chi}{\partial t} = |\tilde{\mathbf{s}}| - E_1 \chi, \quad (6)$$

where E_1 is the viscoelastic spring stiffness, and η_1 is the viscosity in the Kelvin element. The right-hand side of (6) can be interpreted as the macroscopic representation of the viscous effect due to moisture in nano- and micro-pores. It is similar to the hardening

force in plasticity, which represents micro cracking controlled by the equivalent plastic strain.

The viscoplastic strain contribution is expressed according to the formulation proposed by Perzyna (1966). When the yield criterion is violated in the effective stress space, i.e. when $\tilde{f} \geq 0$ with \tilde{f} the yield function, the viscoplastic strain rate is expressed in the associative form as

$$\dot{\boldsymbol{\epsilon}}_{\text{vp}} = \frac{1}{\tau_2} \tilde{\phi} \tilde{f}_{\boldsymbol{\sigma}}, \quad (7)$$

where $\tau_2 = \eta_2 / E_2$ is the viscoplastic relaxation time, η_2 is the corresponding viscosity of the damper element, $\tilde{f}_{\boldsymbol{\sigma}} = \partial \tilde{f} / \partial \tilde{\boldsymbol{\sigma}}$ and the overstress function $\tilde{\phi}$ is given by the following power-law form

$$\tilde{\phi}(\tilde{f}) = \left(\frac{\tilde{f}}{f_t} \right)^N, \quad (8)$$

with f_t the initial tensile strength and N ($N \geq 1$) a real number.

Another important component of our model is the hardening force q which defines the elastic domain of the material and is made a function of both the equivalent plastic and equivalent viscoelastic strains as

$$q(\kappa, \chi) = f_t g(\kappa) h(\chi). \quad (9)$$

The function g is defined here as an exponential softening curve function of the equivalent plastic strain κ in the effective space:

$$g(\kappa) = (1 + a) \exp(-b\kappa) - a \exp(-2b\kappa), \quad (10)$$

with the parameters a and b governing the residual and the slope. The second function is defined by

$$h(\chi) = \left\{ 1 + \chi_a \log \left(\frac{\chi}{\chi_s} \right) \right\}, \quad (11)$$

where, by using the log function, small values of the equivalent viscoelastic strain result in an increase of the tensile strength. This is particularly useful in dynamics where the viscous strain decreases with increasing loading rate. From a physical standpoint, this represents the retardation effect in the nano-pores due to the Stefan effect – the Stefan effect is an increase of tensile strength due to adhesive forces between moisture and skeleton. χ_s is the maximum value of the equivalent viscoelastic strain when the Stefan effect is activated. When the equivalent measure of the viscoelastic strains exceeds this value (no Stefan effect) the log term is negative and the strength is multiplied with a term lower than one and plasticity is activated earlier. Here, we add an additional rate effect to the viscosity terms. The two viscosity

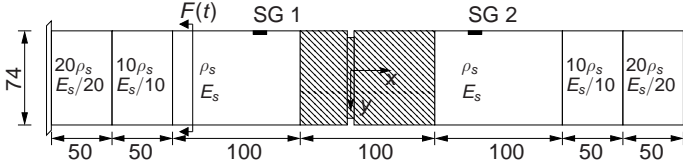


Figure 1: Model of the Split Hopkinson bar test setup (dimensions in mm).

terms reflect microscale processes as the Stefan effect and distributed microcracking. These micromechanical effects are rate dependent. The idea is to incorporate the following rate dependent viscosity relation in the model, similar to what is done in mantle rheology (Becker 2006) and in rate dependent frictional sliding problems (Coker et al. 2005):

$$\eta_i = \eta_i^0 \left(1 + (\dot{\epsilon}_{eq})^{\frac{1-n}{n}} \right). \quad (12)$$

In the above relation, ϵ_{eq} is the equivalent measure of the strain tensor and η_i^0 ($i = 1, 2$) are the viscosities in the elastic and plastic part in case of static loading conditions. In Equation (12) n is a real value ($0 < n \leq 1$). The mesoscopic representation combined with the rate dependent constitutive model is applied to reproduce the results from a Split Hopkinson Bar test.

3 SPLIT HOPKINSON BAR TEST

The Split Hopkinson bar apparatus consists of an incident bar (~ 5 m), the test specimen (0.1 m), and the output bar (~ 5 m). In the computational model the length of the incident and output bars is 250 mm. We apply material based absorbing boundary conditions, see Figure 1. SG 1 refers to the position for strain measurement of the incoming tensile wave while SG 2 indicates the points where the transmitted load pulse is measured. The values for E_s and ρ_s are adjusted to obtain comparable results at SG 1 with respect to the experiments ($E_s = 4572$ MPa, $\rho_s = 1829 \cdot 10^{-11}$ N s²/mm⁴). Identical acoustic impedances $\sqrt{E\rho}$ of the materials is necessary to avoid spurious waves in the response. A detailed description of the experiments can be found in (Rossi et al. 1992; Vegt et al. 2006). For a mesoscopic analysis, an accurate and realistic geometrical model is necessary: the shape, size and distribution of the aggregate particles must resemble real concrete in a statistical sense. There exist specific algorithms for generation of random aggregate structures taking into account the size, shape and spatial distributions (Häfner et al. 2006; Wriggers and Moftah 2006). Here, we use HADES (HADES 2006), a discrete element package that allows for the simulation of granular materials. The individual particles are generated in a non-overlapping way in a region. This region can be

tablenameTable 1: Model parameters.

E_2	38500 MPa
ν	0.2
ρ	$2200 \cdot 10^{-12}$ N s ² /mm ⁴
f_t	3 MPa (matrix)
τ_2	0.08 s
b	500
a	0
α	1
β	1800
E_1	60000 MPa
η_1	10000 MPa s
χ_a	0.2
χ_s	0.00001
n	0.3
N	1
Δt	10^{-8} s

defined by periodic boundaries, rigid boundaries or partly periodic and partly rigid boundaries. Each particle is given an random initial linear and angular velocity. The particles are iteratively displaced to a position that is obtained by integrating the velocity over a small time period. Similarly, the velocity of a particle at the next iteration is calculated by integrating the force or torque that acts on each particle. Gravitational forces, paste friction and contact forces between particles have been implemented. Next, the boundaries can be moved according to user-defined functions. In this way, a number of experiments can be reproduced. Dense packings can be obtained in this way, but it is also possible to move the periodic or rigid walls of the container increasing the volume density of the mixture. In this way arbitrary densities can be obtained up to the maximum density. The output of a two-dimensional simulation can be used to create a distribution of aggregates as shown in Figure 2 and 3.

There are clear differences in the spatial distributions of the aggregates. Three realisations are shown in Figure 2. For realisation (2) the aggregates are concentrated in the middle of the specimen. In the other distributions (1,3), several aggregates are placed close to the free boundaries, and create therefore, potential positions for damage initiation. In realisation (1) particles to the left are closely arranged in a column and failure can develop and propagate in this weak zone. In average, 28000 linear triangular elements are used for the discretisation and a Courant number of approximately 0.75 is ensured with a time step size $\Delta t = 10^{-7}$ s.

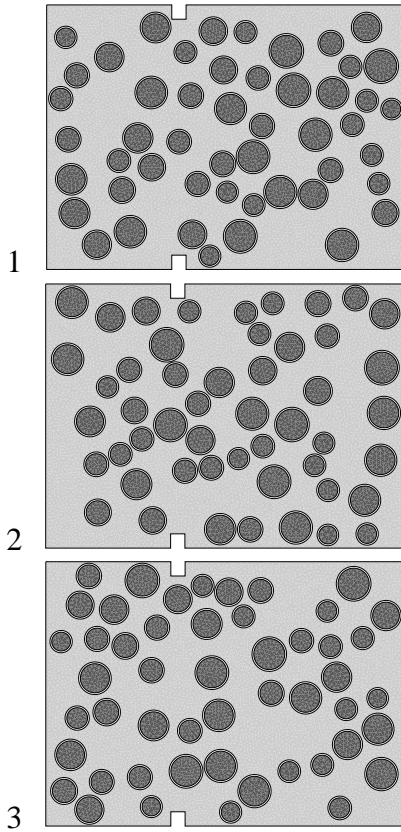


Figure 2: Different realisations of the test specimen. Particle density is 30 %.

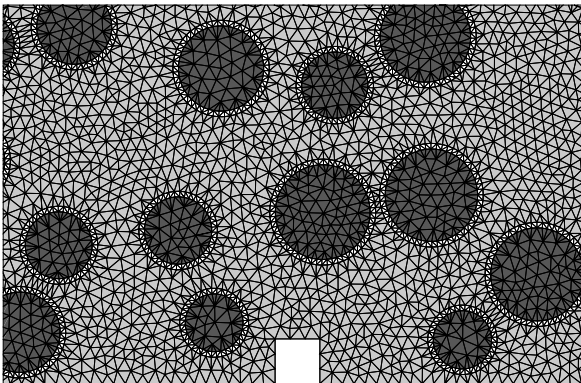
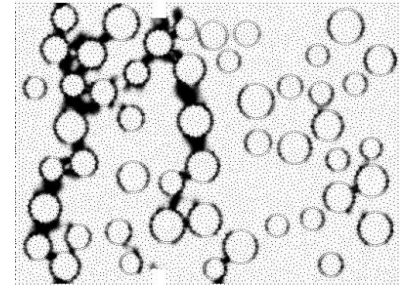
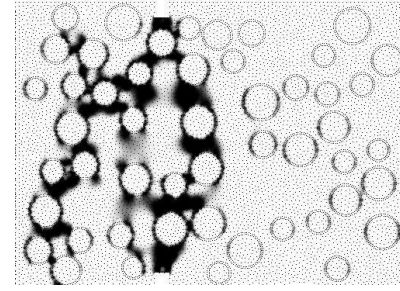


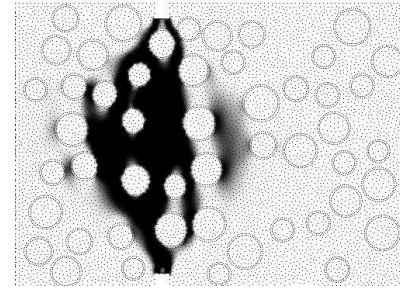
Figure 3: Detail of the finite element discretisation number 3. Light grey is the matrix, the aggregates in dark grey surrounded by the white interfacial transition zones.



$f_t = 1.0$ MPa



$f_t = 2.0$ MPa



$f_t = 3.0$ MPa

Figure 4: Fracture planes corresponding to a different strength of the interfacial transition zone. Configuration 3 is analysed. Black corresponds to damage parameter $\omega = 1$.

4 APPLICATIONS

We test the influence of the tensile strength of the interfacial transition zone and the consequences of different distributions on the overall dynamic tensile strength. Furthermore, the rate dependent properties of the bulk material are changed to examine the influence on failure patterns and the global strength.

4.1 Strength of ITZ

In concrete a gradient in water cement ratio develops around the aggregate particles during casting, resulting in a different microstructure of the surrounding hydrated cement paste. Therefore, the ITZ contains a gradient of porosity and a gradient of properties which is here neglected. Instead we restrict ourselves to variations (1.0, 2.0 and 3.0 MPa) of the tensile strength of the ITZ. When the matrix and ITZ have identical strength the global strength is obviously higher compared to situations with lower strength of the ITZ, see Figure 5. However, it is important to

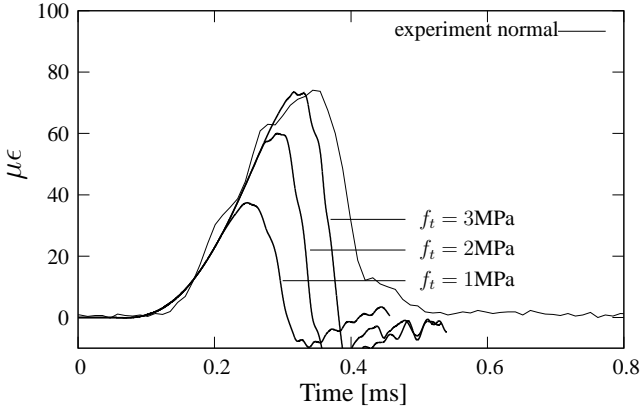


Figure 5: Time-strain curves at the upper bar (SG2). Transmitted pulse and a measure of the strength of the material. The fracture planes are shown in Figure 4.

note the relatively high impact of the ITZ strength on the global strength comparing the number of ITZ elements to the total number of elements in the simulations. Therefore, the most critical points are the ITZs and the mutual connection between ITZs. The experimental result (normal saturation level) is reported in Figure 5. In the mesoscopic model the aggregates are elastic and therefore no direct contribution to the rate effect is present. The fracture planes, represented by the damage parameter ω are shown in Figure 4.

4.2 Different distributions

In Figure 7 the final fracture patterns are shown for different distributions of the aggregates. The tensile strength of the ITZ is 1.0 MPa. In the three distributions the final failure consists of 1-2 fracture planes. For realisation (2) damage initiates at the notches, whereas for (1) and (3) failure is initiated between aggregates and the free boundary. These possible fracture planes can be compared to experimental results (Vegt et al. 2006) for the fracture zone. Figure 8 shows a picture from an optical microscope, where the specimen (impregnated with a fluorescent epoxy) is studied to examine possible microcracks. Figure 6 shows that there is no significant variation of the global tensile strength for different distributions of the particles. The overall tensile strength is obtained by multiplying the strain measurement, see Figure 5, with the Young's modulus of the upper bar.

4.3 Influence of viscosity in bulk material

The previous analysis proved that the initial strength of the interfacial transition zone is an important parameter for the global response of the model. The key parameters in our model are the two viscosity parameters. Next, we fix the material properties for the ITZ and focus on the behaviour of the bulk material by changing viscosity parameter η_1 . This parameter re-

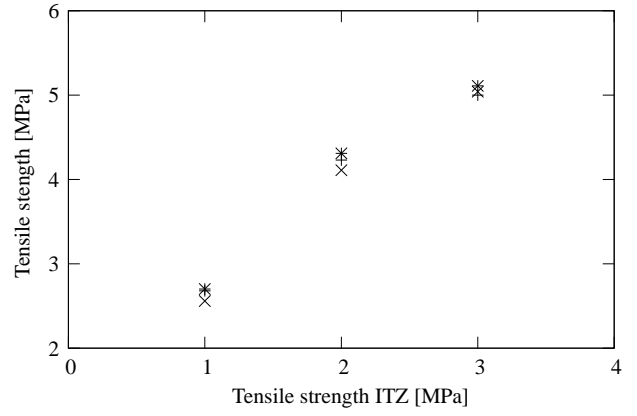


Figure 6: Tensile strength of the concrete specimen as a function of the tensile strength of the ITZ.

flects the Stefan effect and is related to the microstructure via the moisture content and the pore size distribution. The influence of η_1 for the bulk material on the global strength is not significant as shown in Figure 9. We use a wide range of the viscosity parameter to reproduce the different moisture contents from the experiments. An explanation for the less significant influence of the viscoelastic contribution is that

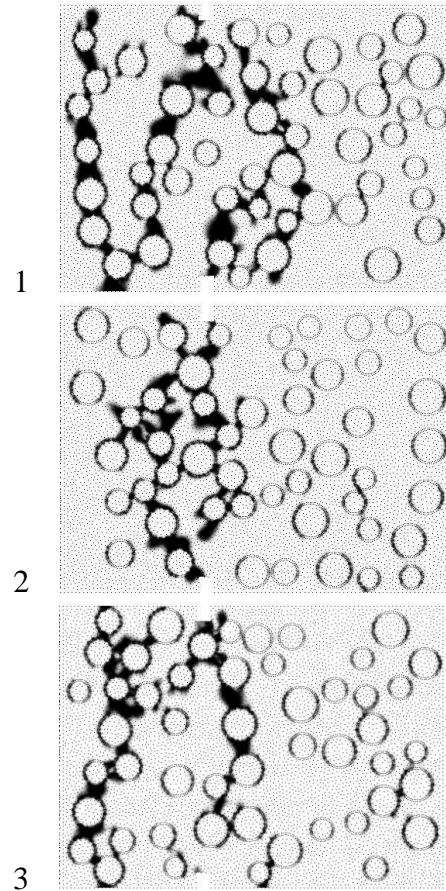


Figure 7: Fracture planes for different realisations. Tensile strength $f_t = 1$ MPa. Black corresponds to damage parameter $\omega = 1$.

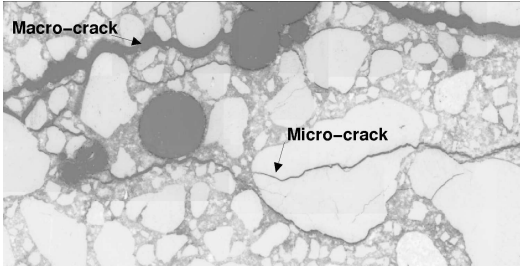
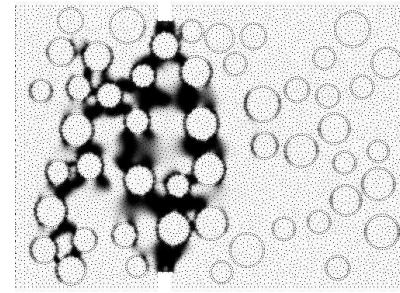
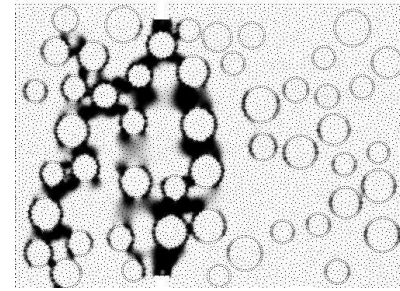


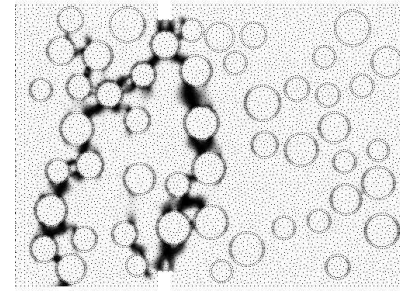
Figure 8: Microscopic picture of the fracture plane from experiment (Vegt et al. 2006).



$$\eta_1 = 10^3 \text{ MPa s}$$



$$\eta_1 = 10^4 \text{ MPa s}$$



$$\eta_1 = 10^6 \text{ MPa s}$$

Figure 10: Fracture planes corresponding to different values of the viscosity. Here only the bulk material is changed. Black corresponds to damage parameter $\omega = 1$.

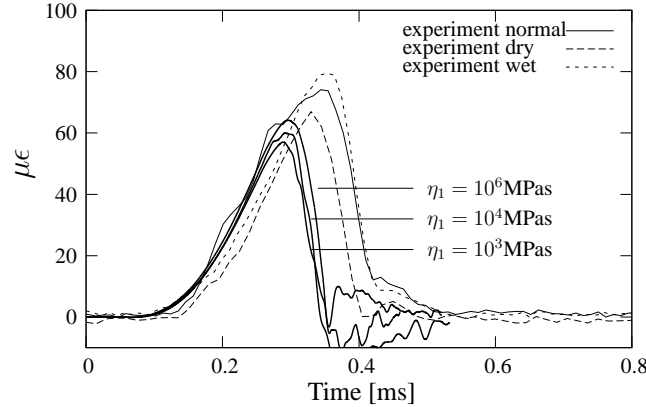


Figure 9: Time-strain curves at the upper bar (SG2) for different viscosities η_1 .

only the viscosity for the matrix material is varied. However, the failure initiates in the weak ITZ elements, where the same viscosity parameter is used for all analyses. Therefore, the weak zones and paths are the same as in the previous analysis and the global strength is not clearly affected by only changing the surrounding bulk material. However, an increase of viscosity in the bulk material reduces the diffusion of damage around the aggregates as a consequence of the increased strength of the material, see Figure 10.

4.4 Influence of viscosity in bulk material and ITZ

We now change the viscosity in the viscoelastic part for both the bulk material and the ITZ. The time strain response is reported in Figure 11. We can compare these results to Figure 9. A clear difference is the increased dependency of the global tensile strength on the viscosity parameter η_1 . Therefore, it is important to properly change the material properties of the ITZ elements as they are the first active elements in the localisation process while the surrounding bulk material is predominantly unloading. However, the overall tendency in the failure process does not change if we compare the final fracture planes in Figure 10 and Figure 12.

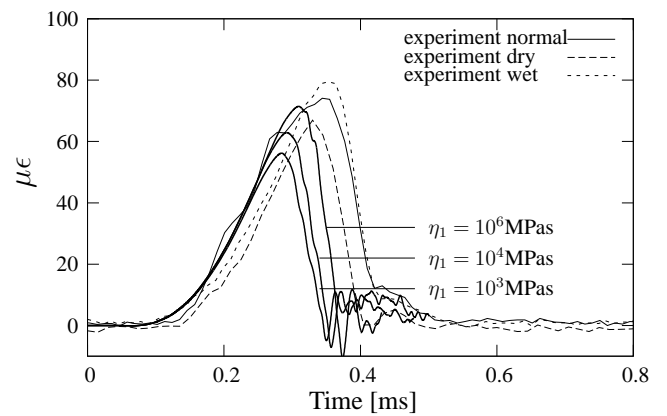
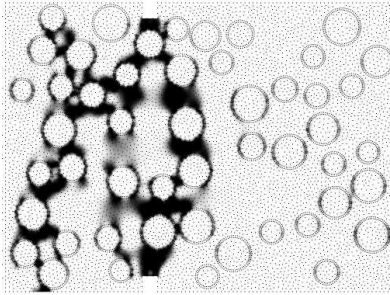


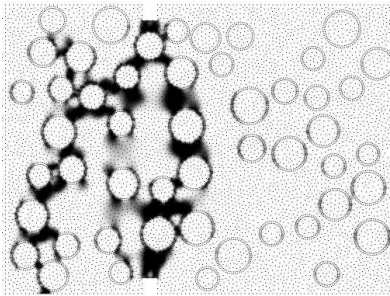
Figure 11: Time-strain curves at the upper bar (SG2) for different viscosities η_1 .

5 CONCLUSIONS

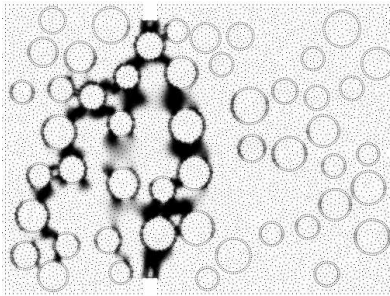
The influence of the heterogeneous mesostructure of concrete on the impact response is analysed. The geometrical model consists of aggregates, interfacial transition zones and a matrix. With this lower level model a more in-depth study on failure mechanisms and inertia effects is possible. The ITZ between aggregate particles and bulk paste plays a major role in the material behaviour of cementitious composites. We observed that the strength of the interfacial transition zone significantly influences the overall tensile strength. Different fracture planes are observed as a consequence of changing the distribution of the aggregates. A small increase of the overall tensile strength was found when changing the rate dependent properties of the bulk material alone. However, when we change the viscosity both for the ITZ and the bulk material a more significant increase of the global tensile strength was observed. Therefore, the rate effect of the material is strongly related to the weakest part of the material, where failure is initiated.



$$\eta_1 = 10^3 \text{ MPa s}$$



$$\eta_1 = 10^4 \text{ MPa s}$$



$$\eta_1 = 10^6 \text{ MPa s}$$

Figure 12: Fracture planes corresponding to different values for the viscosity. Both the material for the bulk and ITZ is changed. Black corresponds to damage parameter $\omega = 1$.

REFERENCES

- Bažant, Z. P. and P. Prat (1988). Microplane model for brittle-plastic material: I. theory. *Journal of Engineering Mechanics* 114, 1672–1688.
- Becker, T. W. (2006). On the effect of temperature and strain-rate dependent viscosity on global mantle flow, net rotation, and plate driving forces. *Geophysical Journal International* 167(2), 943–957.
- Bolander, J. E. and N. Sukumar (2005). Irregular lattice model for quasistatic crack propagation. *Physical Review B* 71, 1–12.
- Camacho, G. T. and M. Ortiz (1996). Computational modelling of impact damage in brittle materials. *International Journal of Solids and Structures* 33(20-22), 2899–2938.
- Carol, I. and Z. P. Bažant (1997). Damage and plasticity in microplane theory. *International Journal of Solids and Structures* 34, 3807–3835.
- Carol, I., C. López, and O. Roal (2001). Micromechanical analysis of quasi-brittle materials using fracture-based interface elements. *International Journal for Numerical Methods in Engineering* 52, 193–215.
- Coker, D., G. Lykotrafitis, A. Needleman, and A. Rosakis (2005). Strain localization and bifurcation in a nonlocal continuum. *Journal of the Mechanics and Physics of Solids* 53, 884–922.
- D’Addetta, G. A., F. Kun, and E. Ramm (2002). On the application of a discrete model to the fracture process of cohesive granular materials. *Granular Matter* 4, 77–90.
- HADES (2006). Habanera’s discrete element simulator. <http://www.habanera.nl/>.
- Häfner, S., S. Eckardt, T. Luther, and C. Könke (2006). Mesoscale modeling of concrete: Geometry and numerics. *Computers and Structures* 84, 450–461.
- Ibrahimbegovic, A. and A. Delaplace (2003). Microscale and mesoscale discrete models for dynamic fracture of structures built of brittle material. *Computers and Structures* 81, 1255–1265.
- Ju, J. W. (1989). On energy-based coupled elastoplastic damage theories: constitutive modeling and computational aspects. *International Journal of Solids and Structures* 25(7), 803–833.
- Kuhl, E., E. Ramm, and K. Willam (2000). Failure analysis of elasto-plastic material models on different levels of observation. *International Journal of Solids and Structures* 37, 7259–7280.
- Lackner, R., C. Hellmich, and H. A. Mang (2002). Constitutive modeling of cementitious materials in the framework of chemoplasticity. *International Journal for Numerical Methods in Engineering* 53, 2357–2388.
- Maiti, S., K. Rangaswamy, and P. H. Geubelle (2005). Mesoscale analysis of dynamic fragmentation of ceramics under tension. *Acta Materialia* 53, 823–834.
- Mühlhaus, H.-B. (1989). Application of Cosserat theory in numerical solutions of limit load problems. *Archive of Applied Mechanics (Ingenieur Archiv)* 59, 124–137.
- Nagai, K., Y. Sato, and T. Ueda (2004). Mesoscopic simulation of failure of mortar and concrete by 2d rbsm. *Journal of Advanced Concrete Technology* 2, 359–374.
- Perzyna, P. (1966). Fundamental problems in viscoplasticity. In *Advances in Applied Mechanics*, Volume 9, pp. 243–377. New York: Academic Press.
- Reinhardt, H. and J. Weerheijm (1991). Tensile fracture of concrete at high loading rates taking account of inertia and crack velocity effects. *International Journal of Fracture* 51, 31–42.
- Rossi, P., J. G. M. van Mier, C. Boulay, and F. L. Maou (1992). The dynamic behaviour of concrete: influence of free water. *Materials and Structures/Matériaux et Constructions* 25, 509–514.
- Schlengen, E. and J. G. M. van Mier (1992). Simple lattice model for numerical simulation of fracture of concrete materials and structures. *Materials and Structures/Matériaux et Constructions* 25, 534–542.
- Sercombe, J., F.-J. Ulm, and H.-A. Mang. (2000). Consistent return mapping algorithm for chemoplastic constitutive laws with internal couplings. *International Journal for Numerical Methods in Engineering* 47, 75–100.
- Simone, A. and L. J. Sluys (2004). The use of displacement discontinuities in a rate-dependent medium. *Computer Methods in Applied Mechanics and Engineering* 193, 3015–3033.
- Tijssens, M. G. A., L. J. Sluys, and E. van der Giessen (2001). Simulation of fracture of cementitious composites with explicit modeling of microstructural features. *Engineering Fracture Mechanics* 68, 1254–1263.
- Ulm, F.-J. and O. Coussy (1995). Modelling of thermochemomechanical couplings of concrete at early ages. *Journal of Engineering Mechanics* 121, 785–794.
- Vegt, I., J. Weerheijm, R. R. Pedersen, and L. J. Sluys (2006, 27–30 March). Modelling of impact behaviour of concrete - an experimental approach. In G. Meschke, R. de Borst, H. A. Mang, and N. Bićanić (Eds.), *Computational Modelling of Concrete Structures – EURO-C 2006*, Mayrhofen, Tyrol, Austria. Taylor & Francis, London/Leiden/New York/Philadelphia/Singapore.
- Wriggers, P. and S. Moftah (2006). Mesoscale models for concrete: Homogenisation and damage behaviour. *Finite Elements in Analysis and Design* 42, 623–636.